

Adjoint-optimized nanoscale light extractor for nitrogen-vacancy centers in diamond

Raymond A. Wambold¹, Zhaoning Yu^{1,2}, Yuzhe Xiao¹, Benjamin Bachman³, Gabriel Jaffe², Shimon Kolkowitz², Jennifer T. Choy^{4,1,5}, Mark Eriksson², Robert J. Hamers³, Mikhail A. Kats^{1,2,5}

1. Department of Electrical and Computer Engineering, University of Wisconsin – Madison

2. Department of Physics, University of Wisconsin – Madison

3. Department of Chemistry, University of Wisconsin – Madison

4. Department of Engineering Physics, University of Wisconsin – Madison

5. Department of Materials Science and Engineering, University of Wisconsin - Madison

Abstract

We designed a nanoscale light extractor (NLE) for the efficient outcoupling and beaming of broadband light emitted by shallow, negatively charged nitrogen-vacancy (NV) centers in bulk diamond. The NLE consists of a patterned silicon layer on diamond and requires no etching of the diamond surface. Our design process is based on adjoint optimization using broadband time-domain simulations, and yields structures that are inherently robust to positioning and fabrication errors. Our NLE functions like a transmission antenna for the NV center, enhancing the optical power extracted from an NV center positioned 10 nm below the diamond surface by a factor of more than 35, and beaming the light into a 30° cone in the far field. This approach to light extraction can be readily adapted to other solid-state color centers.

Introduction

Negatively charged nitrogen-vacancy (NV) centers in diamond are optical emitters whose level-structure is highly sensitive to external perturbations, which makes them excellent sensors of highly localized electric and magnetic fields, temperature, and strain [1]–[5]. NV centers are of great interest for quantum computing and communication [6]–[10] and the study of quantum phenomena such as quantum entanglement and superposition [11], [12]. However, efficiently extracting NV fluorescence is often challenging due to the high index of refraction in diamond (~ 2.4), which results in high reflectance at the diamond-air interfaces and total internal reflection for emission angles larger than the critical angle. Previous attempts to extract more light from bulk diamond primarily involved the etching of the diamond itself (a complicated fabrication process that can adversely affect NV properties such as spin coherence) [13]–[19] or fabricating structures that still required a high numerical aperture oil-immersion objective to efficiently collect the emission (which adds system complexity and is detrimental to sensing applications) [20]–[24]. Furthermore, precision etching of diamond around NV centers can be a substantial challenge and can damage the surface of diamond, resulting in roughness and modifying the chemical termination [25], which can degrade the quantum properties of NV centers [26], [27].

Here, we design a silicon-based nanoscale light extractor (NLE) that sits on the top of a flat, un-patterned diamond surface and can enhance the optical output of near-surface NV emitters by more than 35× compared to the unpatterned case, directing the light into a narrow cone that can be easily collected with low-NA optical systems. Our NLE consists of a patterned silicon structure on top of the diamond surface (Fig. 1), directly above a shallow NV center (< 300 nm below the surface). The proximity of a resonant high-index dielectric structure close to the emitter enables near-field coupling to and broadband Purcell enhancement of the emitter [24], [28]. We designed the silicon NLE using an adjoint-optimization method,

optimizing for NV emission funneled into a 30° cone into the far field. This approach both increases collection efficiency and enhances the radiative emission rate of the NV center.

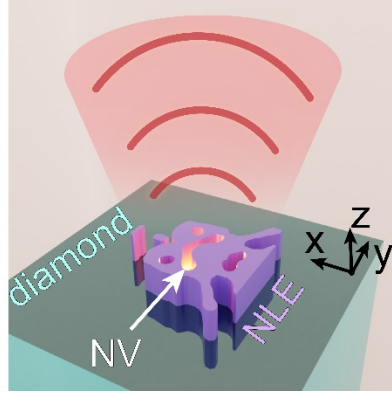


Figure 1. Schematic of the nanoscale light extractor (NLE), which sits on the diamond surface above an NV center and directs fluorescence out of the diamond and into a narrow cone in the far field. In this figure, the schematic is a render of the actual optimized structure reported below.

Design

Our approach focuses on broadband emission enhancement of negatively charged NV centers close to the diamond surface, which is especially useful for sensing applications in which measurement sensitivity is limited by the number of collected photons across the entire NV emission spectrum.

Negatively charged NV centers in bulk diamond have optical transitions at ~637 nm (location of the zero phonon line in the spectrum), but fluoresce over a bandwidth of >150 nm due to vibrational side bands in the diamond [29], [30]. Therefore, we define a spectrum-averaged figure of merit (*FoM*) to quantify the degree of light extraction:

$$FoM = \frac{\int I_{NV}(\lambda) \times \eta(\lambda) d\lambda}{\int I_{NV}(\lambda) d\lambda} \quad (1)$$

Here, $I_{NV}(\lambda)$ is the normalized emission spectrum of the NV centers in bulk diamond taken from ref. [31] and $\eta(\lambda)$ is the extraction efficiency of our NLE, which is defined as the number of photons emitted into free-space in the presence of the NLE divided by the number of photons emitted into free-space by that same NV (i.e., same depth and same orientation) with no NLE present, at a wavelength λ . Note that $\eta(\lambda)$ includes both collection and Purcell enhancements. For example, an NLE that results in 10 times as many photons emitted into free space at every wavelength would have $\eta(\lambda) = 10$ and $FoM = 10$.

For all plots in this paper, the bounds of the integral in Eqn. (1) are set to 635 – 800 nm to cover the entire range of NV emission. Our NLE achieves broadband NV fluorescence enhancement, in particular for sensing applications using shallow NVs, but the design approach can readily be adapted to focus on more-narrow spectral ranges (e.g., the zero-phonon line).

To design a high-performance NLE, we used adjoint optimization—a design technique that has been used extensively in mechanical engineering and has recently been applied to the design of optical metasurfaces and other photonic structures [32]–[34]. The optimization process consists of the evolution of the structure,

defined by a refractive-index profile $n(\mathbf{r}, \lambda)$, towards maximizing the overlap between a forward simulation field [$E_{\text{fwd}}(\mathbf{r}, \lambda)$] and a specific adjoint simulation field [$E_{\text{adj}}(\mathbf{r}, \lambda)$], where \mathbf{r} is a position within the structure. We used finite-difference time-domain (FDTD) simulations (implemented in Lumerical FDTD [35]) to determine the forward and adjoint fields in the optimization region across the spectrum of interest. At each optimization generation, a figure-of-merit gradient is calculated according to [36]:

$$G(\mathbf{r}, \lambda) \propto n(\mathbf{r}, \lambda) \cdot \text{Re}[E_{\text{fwd}}(\mathbf{r}, \lambda) \cdot E_{\text{adj}}(\mathbf{r}, \lambda)] \quad (2)$$

A positive value of $G(\mathbf{r}, \lambda)$ indicates that a small increase in the refractive index $n(\mathbf{r}, \lambda)$ at position \mathbf{r} will result in a stronger overlap between the forward and adjoint fields. Because it is typically not possible to separately engineer the index at different wavelengths, we define a wavelength-weighted gradient:

$$G(\mathbf{r}) = \frac{1}{\Delta\lambda} \int I_{NV}(\lambda) G(\mathbf{r}, \lambda) d\lambda \quad (3)$$

$G(\mathbf{r})$ is then used to update the index profile according to $n_{\text{new}}(\mathbf{r}, \lambda) = n_{\text{old}}(\mathbf{r}, \lambda) + c \cdot G(\mathbf{r})$ where c is a normalization constant.

Figure 2(A) shows the design process for our NLE. To start, the optimization is seeded with a random continuous complex refractive index taking values between that of air ($n_{\text{air}} = 1$) and silicon ($n_{\text{Si}}(\lambda)$ between 3.85 and 3.69), calculated by $n(\mathbf{r}, \lambda) = p(\mathbf{r}) \cdot n_{\text{Si}}(\lambda) + [1 - p(\mathbf{r})] \cdot n_{\text{air}}$ where $p(\mathbf{r})$ ranges between 0 and 1, such that if $p = 1$, then $n = n_{\text{Si}}$. Our forward simulations are sourced by an electric dipole 10 nm below the diamond surface, with the dipole moment oriented in the XZ plane and tilted at an angle of 54.7° off the Z axis to mimic the orientation of the NV emitter in [100] diamond [29]. The adjoint simulations are sourced by a Gaussian beam with a diffraction angle of ±15° injected toward the diamond surface along the Z axis. The beam was set to mimic a time-reversed emission beam that can be collected by an objective with $\text{NA} < 0.4$.

To design a structure that can realistically be fabricated, there should ideally be no material variance in the vertical (Z) direction. We impose this constraint in our optimization by 1) forcing the index in a single column along Z to be constant and 2) averaging $G(\mathbf{r})$ along each column during the update step such that a singular G is applied to each column given by $G(\bar{\mathbf{r}}) = \int_{z_{\min}}^{z_{\max}} G(\mathbf{r}) / (z_{\max} - z_{\min}) dz$ (similar to e.g., ref. [36]), with $\bar{\mathbf{r}}$ being the two-dimensional position vector in the (x, y) plane.

The optimization method described above yields an optimized profile $p(\bar{\mathbf{r}})$ corresponding to a continuum of index values $n(\bar{\mathbf{r}}, \lambda)$. To evolve the index distribution into a binary structure of silicon and air that can be made by lithography and etching, and also ensuring that the feature sizes are not too small, we followed the methods of Sigmund in ref. [37]. This approach applies a conically shaped blurring function to the index matrix at each iteration to smooth the index distribution to remove features that are smaller than the cone radius, R . For our optimization we used a conical function with a maximum radius of 36 nm to result in structures that can be readily made with most electron-beam lithography systems. The new blurred profile $p_{\text{blur}}(\bar{\mathbf{r}})$, is created according to [37]:

$$p_{\text{blur}}(\bar{\mathbf{r}}) = \int \frac{w(\bar{\mathbf{r}}, \bar{\mathbf{r}}') \cdot p(\bar{\mathbf{r}})}{w(\bar{\mathbf{r}}, \bar{\mathbf{r}}')} d\bar{\mathbf{r}}' \quad (4)$$

$$w(\bar{\mathbf{r}}, \bar{\mathbf{r}}') = \begin{cases} 0, & \|\bar{\mathbf{r}}' - \bar{\mathbf{r}}\| > R \\ R - \|\bar{\mathbf{r}}' - \bar{\mathbf{r}}\|, & \|\bar{\mathbf{r}}' - \bar{\mathbf{r}}\| \leq R \end{cases} \quad (5)$$

where $w(\bar{\mathbf{r}}, \bar{\mathbf{r}}')$ is a weight function that becomes larger closer to position $\bar{\mathbf{r}}$. In addition to blurring, a binary push function is required to finish the optimization with a fully binary structure (i.e., in our case, at each point in the optimization region the final material should be either air or silicon). The binarization method found in ref. [37] and [34] was the guide for our implementation. Specifically, this method modifies the blurred element matrix as follows:

$$p_{\text{bin}}(\bar{\mathbf{r}}) = \begin{cases} \alpha e^{-\frac{\beta(\alpha - p_{\text{blur}}(\bar{\mathbf{r}}))}{\alpha}} - (\alpha - p_{\text{blur}}(\bar{\mathbf{r}}))e^{-\beta}, & 0 \leq p(\bar{\mathbf{r}}) \leq \alpha \\ 1 - (1 - \alpha)e^{-\frac{\beta(p_{\text{blur}}(\bar{\mathbf{r}}) - \alpha)}{1 - \alpha}} - (\alpha - p_{\text{blur}}(\bar{\mathbf{r}}))e^{-\beta}, & \alpha < p(\bar{\mathbf{r}}) \leq 1 \end{cases} \quad (6)$$

where $p_{\text{bin}}(\bar{\mathbf{r}})$ is the modified (new) value of p at position $\bar{\mathbf{r}}$. Here, α is a cutoff parameter that allows us to define dilated and eroded edges (to account for fabrication errors), but is set to the midpoint value of 0.5 during the optimization process. The parameter β controls the strength of binarization applied to the structure. A β -value of 0 gives no increased binarization to the structure leading to $p_{\text{bin}} = p$. As β increases, values of $p < \alpha$ are pushed towards zero while values of $p > \alpha$ are pushed towards one. As the optimization progresses, the value of β is increased to provide a binary structure by the end of the optimization [~iteration 200 in Fig. 2(C)]. At each iteration, our simulated structure is the result of first blurring and then applying the binarization filter to the final structure at the previous step.

We leveraged the inherently broadband nature of the FDTD method to simulate and optimize the performance of our device across the entire NV emission spectrum, simultaneously achieving a design that is robust to errors in fabrication. Previous works using adjoint optimization with a frequency-domain electromagnetic solver achieve fabrication robustness through simulating dilated and eroded devices each iteration, which corresponds to a three-fold increase in the number of simulations required [34], [38]–[40]. In our optimizations, fabrication robustness was built-in automatically due our requirement for broadband performance together with the scale invariance of Maxwell’s equations (i.e., larger structures at longer wavelength behave similarly to smaller structures at shorter wavelength). This correspondence between broadband performance and shape robustness has been observed previously for other inverse-design approaches [41], [42].

To find the ideal height, we first ran a series of a series of 2D optimizations, sweeping over a range of heights. Like in the later 3D simulations, the 2D simulations was set up with the dipole embedded 10 nm into diamond and oriented in the XY plane at an angle of 54.7° above the X Axis. We swept the height from 50 to 900 nm in steps of 50 nm and ran 20 optimization runs for each height. Figure 2(B) shows the average of our *FoM* for each height, with the oscillations reminiscent of Fabry-Perot fringes. The maximum *FoM* occurs at a height of approximately 200 nm. Based on these results, we decided to run the full 3D optimization of the NLE for a height of 220 nm, noting that 220 nm is a commonly used device-layer

thickness in silicon-on-insulator (SOI) technology [43]. SOI lends itself well to fabricating this structure: crystalline silicon device layers can be transferred to diamond using membrane-transfer techniques [44]. Note that in both the 2D and 3D optimization runs presented here, the integration range of Eqn. (3) was set to be 650 to 800 nm, though the final result is substantially broader, and we always integrated our *FoM* (defined in Eqn. 1) from 635 nm to 800 nm.

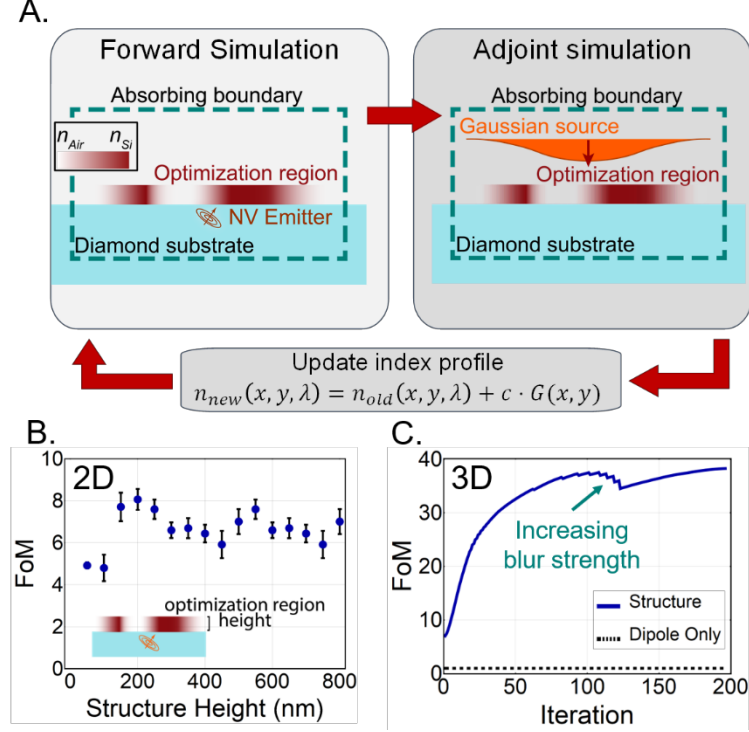


Figure 2. **A.** Visualization of the optimization routine, which evolves an index profile situated above an NV emitter. In the forward simulation, the light source is a dipole at the location of the NV. The source in the adjoint simulation is a Gaussian injected from free space toward the structure. The sensitivity gradient, $G(\vec{r}) = G(x, y)$, is calculated and then used to evolve the index profile. The updated profile is then used in the next iteration. **B.** A sweep of the structure height (i.e., the thickness of the Si membrane), running many full 2D optimization cycles for each height. We found a height of approximately 200 nm to be optimal over the range of the sweep. **C.** *FoM* vs. the iteration number for a full 3D optimization run to generate our NLE. The dips are due to the increase of blurring.

The full 3D optimization run can be seen in Fig. 2(C). The *FoM* increases as the optimization progresses, with occasional dips due to the implementation of our blurring function. The blurring function increases in radius from 4 nm to the maximum of 36 nm in steps of 4 nm as the optimization progress, reaching its maximum at iteration 125. We chose this method of blurring to give the optimization as much freedom as possible in the early iterations but still enforce fabricable features in the final device. The optimization terminates when the device is sufficiently binarized, such that the structure is entirely comprised of air and silicon.

Results

The structure of our optimized NLE is shown in Fig. 3(A), with the extraction efficiency in Fig. 3(B). Though the NLE was optimized for an NV depth of 10 nm, we also show the results for depths of 5 and 15 nm but with the same NLE structure. The normalized transmittance increases for NVs closer to the structure

due to increased coupling with the NLE, which leads to larger Purcell enhancement [45]. For an NV depth of 10 nm, the Purcell enhancement of our device is ~ 7 , averaged across the emission spectrum. Figure 3(C, D) shows the near- and far-field radiation patterns. The NLE can shape the emitted fields from the dipole into a beam that is approximately Gaussian. The fields in Fig. 3(C,D) are for a wavelength of 675 nm, but the beaming persists across the NV spectrum and the peak emission angle does not deviate by more than $\pm 5^\circ$ from the normal (see supplemental S3 for details).

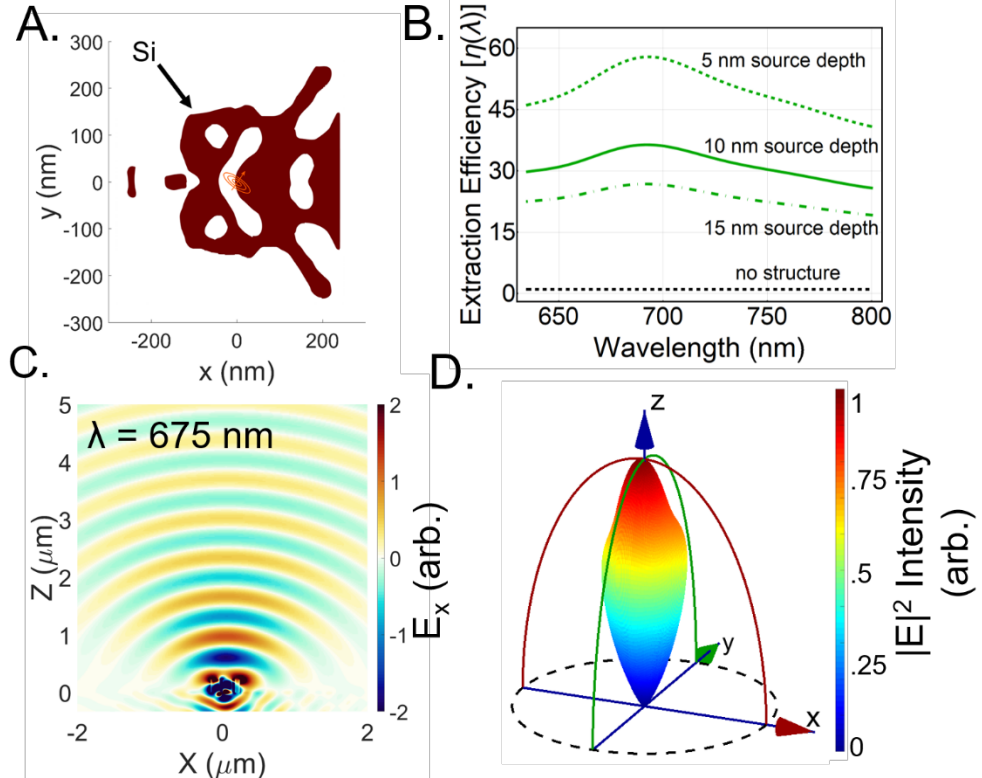


Figure 3. **A.** Top-down view of the final NLE, optimized for an NV depth of 10 nm. **B.** Extraction efficiency [$\eta(\lambda)$] of the NLE for NV depths of 5, 10, and 15 nm below the diamond/air interface. **C,D.** Near and meso-field (x component) of the emitted electric field (**C**) and far-field radiation pattern (**D**) at a wavelength of 675 nm. The beamed power fits well within a 30° cone in the far field.

Due to the broadband spectrum incorporated into the optimization, our devices display considerable tolerance to various fabrication defects as well as robustness to alignment errors (Fig. 4). Though our optimized NLE structure was based on a fixed NV depth of 10 nm, we also simulated its performance for a variety of depths [Fig. 4(A)]. The NLE performs better as the dipole gets closer to the surface due to enhanced coupling. The performance falls off by a factor of 2 at a depth of 25 nm, yet still maintains enhancements of about 15 times the emission of an NV with no NLE. Even down to a dipole depth of 300 nm, the NLE is able to increase the output of the NV by a factor of 3. Note that for NVs at depths substantially different than 10 nm, a more-effective design can very likely be found using the optimization method described above.

The NLE shows minimal performance loss from errors in rotational alignment in the range of -20° to $+20^\circ$ [Fig. 4(B)]. The full 360° rotational plot can be found in the supplemental (S2). We also tested the case where the NLE was offset by some amount from the central dipole position [Fig. 4(D)], and found that the *FoM* remains above 25 for horizontal offsets from -15 to $+30$ nm and for vertical offsets of ± 30 nm.

Furthermore, the structure is more forgiving for dipole locations slightly behind (along x) the large central Si feature, which means that one may want to align the NLE to a position slightly behind the target NV.

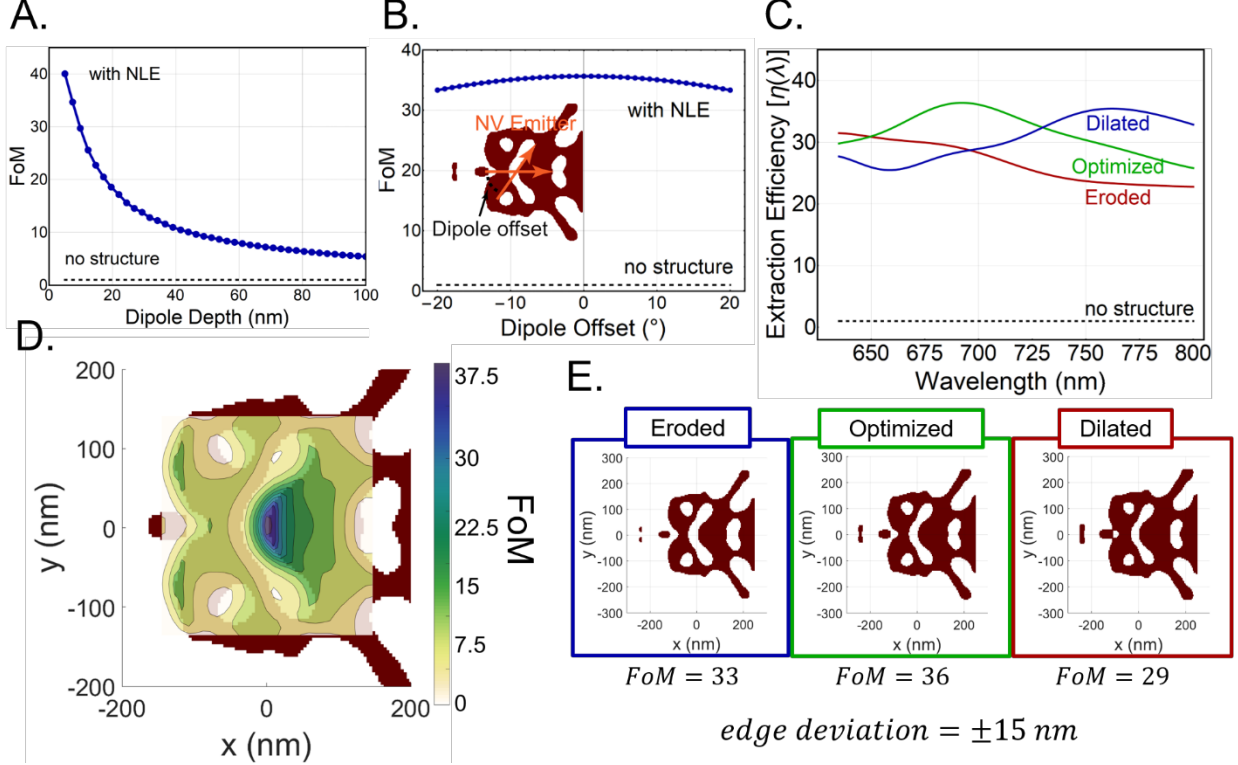


Figure 4. **A.** The NLE maintains good performance through a range of depths, with increasing FoM for NVs closer to the surface. **B.** FoM dependence on the NV emitter angle emulating angular alignment errors of the NLE. **C.** Demonstration of the fabrication robustness of the optimized device for an NV depth of 10 nm. Eroded and dilated structures are based on the optimized structure with edge deviation of ± 15 nm to represent fabrication under/over-etching, respectively. Due to the broadband nature of our optimization, the NLE shows strong tolerance to fabrication errors. **D.** Tolerance of the NLE to lateral offsets of the NV center. The FoM remains above 25 for horizontal offsets from -15 to +30 nm and for vertical offsets of ± 30 nm. **E.** The geometries of the eroded, optimized, and dilated devices simulated in c. The edge deviation refers to how far the edges shifted inward for the eroded or outward for the dilated cases.

In practice, one can reasonably expect the fabrication process to cause deviations in edge locations, e.g., due to proximity effects [46]. Figure 4(C) shows our eroded, optimized, and dilated structures with their normalized transmittance spectra. We calculated the deviated structures by applying a gaussian blurring filter across the optimized pattern, and then selecting cutoff points of the blurred edges to yield new binarized structures. Here, we selected the blur and cutoff to yield edge deviations of ± 15 nm. The NLE maintains good performance across the spectrum despite erosion or dilation [Fig. 2(B)].

It is instructive to compare the FoM of our NLE (~ 35 for NVs at a depth of 10 nm) with some existing structures in the literature designed for broadband vertical outcoupling of light from a diamond slab, with the understanding that the FoM combines the distinct collection-enhancement and Purcell mechanisms.

Dielectric structures comprising etched diamond typically do not provide much Purcell enhancement and include bullseye gratings [21], vertical nanowires [47], solid-immersion metalenses [19], and parabolic reflectors [13]; we estimate that these structures have calculated FoMs of approximately 10 to 20 due entirely to collection enhancement. Resonant geometries proposed thus far have primarily relied on plasmonic enhancement in structures such as metallic cavities [14], [48] and gratings [49], with FoMs of up to \sim 35. The theoretical FoM of resonant metal-dielectric structures in ref. [50] can be well above 100 due to large Purcell enhancement, but the implementation would require elaborate fabrication including filling etched diamond apertures with metal, and the small mode volume limits the positioning tolerance of the NV center to within \sim 5 nm of the field maximum. Finally, note that unlike all of the aforementioned designs, our NLE does not require etching of the diamond, and can be fabricated by using Si membrane transfer techniques [44], [51] or direct CVD growth of Si on a diamond substrate.

Conclusion

We presented a nanoscale light extractor (NLE) designed using adjoint-optimization methods with time-domain simulations to enhance the broadband emission of NV centers in diamond. Our design not only enhances the fluorescence of the NV centers but also demonstrates exceptional beam-shaping qualities, enabling efficient collection with a low-NA lens in free space. Even given reasonable uncertainty in NV center localization and errors in device fabrication, simulations show the NLE maintains a high extraction efficiency. Our results suggest that such robustness to positioning and fabrication errors can be automatically achieved when optimizing for a broadband figure of merit. The NLE can be fabricated with conventional electron-beam lithography techniques without etching of the diamond surface. Our approach can easily be extended to other color centers in diamond, as well as material systems where increased light extraction from defect centers is desired, such as silicon carbide or hexagonal boron nitride [52], [53].

Acknowledgements

This material is based upon work supported by the National Science Foundation under Grant No. CHE-1839174. RW acknowledges support through the DoD SMART program and a scholarship from the Directed Energy Professional Society. Additional contributions by JTC and SK were supported by the U.S. Department of Energy (DOE), Office of Science, Basic Energy Sciences (BES) under Award #DE-SC0020313.

References

- [1] F. Jelezko and J. Wrachtrup, “Single defect centres in diamond: A review,” *Phys. status solidi*, vol. 203, no. 13, pp. 3207–3225, Oct. 2006, doi: 10.1002/pssa.200671403.
- [2] R. Schirhagl, K. Chang, M. Loretz, and C. L. Degen, “Nitrogen-Vacancy Centers in Diamond: Nanoscale Sensors for Physics and Biology,” *Annu. Rev. Phys. Chem.*, vol. 65, no. 1, pp. 83–105, Apr. 2014, doi: 10.1146/annurev-physchem-040513-103659.
- [3] I. Aharonovich and E. Neu, “Diamond Nanophotonics,” *Adv. Opt. Mater.*, vol. 2, no. 10, pp. 911–928, Oct. 2014, doi: 10.1002/adom.201400189.
- [4] L. Rondin, J.-P. Tetienne, T. Hingant, J.-F. Roch, P. Maletinsky, and V. Jacques, “Magnetometry with nitrogen-vacancy defects in diamond,” *Reports Prog. Phys.*, vol. 77, no. 5, p. 056503, May 2014, doi: 10.1088/0034-4885/77/5/056503.
- [5] J. F. Barry *et al.*, “Sensitivity optimization for NV-diamond magnetometry,” *Rev. Mod. Phys.*, vol.

92, no. 1, p. 015004, Mar. 2020, doi: 10.1103/RevModPhys.92.015004.

- [6] L. Childress and R. Hanson, “Diamond NV centers for quantum computing and quantum networks,” *MRS Bulletin*, vol. 38, no. 2. Cambridge University Press, pp. 134–138, Feb. 2013, doi: 10.1557/mrs.2013.20.
- [7] A. Russo, E. Barnes, and S. E. Economou, “Photonic graph state generation from quantum dots and color centers for quantum communications,” *Phys. Rev. B*, vol. 98, no. 8, p. 085303, Aug. 2018, doi: 10.1103/PhysRevB.98.085303.
- [8] A. Beveratos, R. Brouri, T. Gacoin, A. Villing, J. P. Poizat, and P. Grangier, “Single Photon Quantum Cryptography,” *Phys. Rev. Lett.*, vol. 89, no. 18, p. 187901, 2002, doi: 10.1103/PhysRevLett.89.187901.
- [9] F. Jelezko, T. Gaebel, I. Popa, M. Domhan, A. Gruber, and J. Wrachtrup, “Observation of coherent oscillation of a single nuclear spin and realization of a two-qubit conditional quantum gate,” *Phys. Rev. Lett.*, vol. 93, no. 13, p. 130501, Sep. 2004, doi: 10.1103/PhysRevLett.93.130501.
- [10] M. V. Gurudev Dutt *et al.*, “Quantum register based on individual electronic and nuclear spin qubits in diamond,” *Science (80-.).*, vol. 316, no. 5829, pp. 1312–1316, Jun. 2007, doi: 10.1126/science.1139831.
- [11] B.-C. Ren and F.-G. Deng, “Hyperentanglement purification and concentration assisted by diamond NV centers inside photonic crystal cavities,” *Laser Phys. Lett.*, vol. 10, no. 11, p. 115201, Oct. 2013, doi: 10.1088/1612-2011/10/11/115201.
- [12] K. Fang *et al.*, “High-sensitivity magnetometry based on quantum beats in diamond nitrogen-vacancy centers,” *Phys. Rev. Lett.*, vol. 110, no. 13, p. 130802, Mar. 2013, doi: 10.1103/PhysRevLett.110.130802.
- [13] N. H. Wan *et al.*, “Efficient Extraction of Light from a Nitrogen-Vacancy Center in a Diamond Parabolic Reflector,” *Nano Lett.*, vol. 18, no. 5, pp. 2787–2793, May 2018, doi: 10.1021/acs.nanolett.7b04684.
- [14] J. T. Choy *et al.*, “Enhanced single-photon emission from a diamond–silver aperture,” *Nat. Photonics*, vol. 5, no. 12, pp. 738–743, Dec. 2011, doi: 10.1038/nphoton.2011.249.
- [15] T. Schröder, F. Gädeke, M. J. Banholzer, and O. Benson, “Ultrabright and efficient single-photon generation based on nitrogen-vacancy centres in nanodiamonds on a solid immersion lens,” *New J. Phys.*, vol. 13, 2011, doi: 10.1088/1367-2630/13/5/055017.
- [16] P. Siyushev *et al.*, “Monolithic diamond optics for single photon detection,” *Appl. Phys. Lett.*, vol. 97, no. 24, p. 241902, Dec. 2010, doi: 10.1063/1.3519849.
- [17] A. Faraon, P. E. Barclay, C. Santori, K.-M. C. Fu, and R. G. Beausoleil, “Resonant enhancement of the zero-phonon emission from a colour centre in a diamond cavity,” *Nat. Photonics*, vol. 5, no. 5, pp. 301–305, May 2011, doi: 10.1038/nphoton.2011.52.
- [18] J. P. Hadden *et al.*, “Strongly enhanced photon collection from diamond defect centers under microfabricated integrated solid immersion lenses,” *Appl. Phys. Lett.*, vol. 97, no. 24, p. 241901, Dec. 2010, doi: 10.1063/1.3519847.
- [19] T. Y. Huang *et al.*, “A monolithic immersion metalens for imaging solid-state quantum emitters,” *Nat. Commun.*, vol. 10, no. 1, pp. 1–8, Dec. 2019, doi: 10.1038/s41467-019-10238-5.

- [20] J. Zheng, A. C. Liapis, E. H. Chen, C. T. Black, and D. Englund, “Chirped circular dielectric gratings for near-unity collection efficiency from quantum emitters in bulk diamond,” *Opt. Express*, vol. 25, no. 26, p. 32420, Dec. 2017, doi: 10.1364/oe.25.032420.
- [21] L. Li *et al.*, “Efficient Photon Collection from a Nitrogen Vacancy Center in a Circular Bullseye Grating,” *Nano Lett.*, vol. 15, no. 3, pp. 1493–1497, Mar. 2015, doi: 10.1021/nl503451j.
- [22] S. Schietinger, M. Barth, T. Aichele, and O. Benson, “Plasmon-enhanced single photon emission from a nanoassembled metal - Diamond hybrid structure at room temperature,” *Nano Lett.*, vol. 9, no. 4, pp. 1694–1698, Apr. 2009, doi: 10.1021/nl900384c.
- [23] S. I. Bogdanov *et al.*, “Ultrabright Room-Temperature Sub-Nanosecond Emission from Single Nitrogen-Vacancy Centers Coupled to Nanopatch Antennas,” *Nano Lett.*, vol. 18, no. 8, pp. 4837–4844, Aug. 2018, doi: 10.1021/acs.nanolett.8b01415.
- [24] M. Y. Shalaginov *et al.*, “Enhancement of single-photon emission from nitrogen-vacancy centers with TiN/(Al,Sc)N hyperbolic metamaterial,” *Laser Photon. Rev.*, vol. 9, no. 1, pp. 120–127, Jan. 2015, doi: 10.1002/lpor.201400185.
- [25] P. Latawiec, M. J. Burek, Y.-I. Sohn, and M. Lončar, “Faraday cage angled-etching of nanostructures in bulk dielectrics,” *J. Vac. Sci. Technol. B, Nanotechnol. Microelectron. Mater. Process. Meas. Phenom.*, vol. 34, no. 4, p. 041801, Jul. 2016, doi: 10.1116/1.4944854.
- [26] S. Sangtawesin *et al.*, “Origins of Diamond Surface Noise Probed by Correlating Single-Spin Measurements with Surface Spectroscopy,” *Phys. Rev. X*, vol. 9, no. 3, p. 031052, Sep. 2019, doi: 10.1103/PhysRevX.9.031052.
- [27] M. Kaviani, P. Deák, B. Aradi, T. Frauenheim, J. P. Chou, and A. Gali, “Proper surface termination for luminescent near-surface NV centers in diamond,” *Nano Lett.*, vol. 14, no. 8, pp. 4772–4777, Aug. 2014, doi: 10.1021/nl501927y.
- [28] J. Riedrich-Möller *et al.*, “Nanoimplantation and Purcell enhancement of single nitrogen-vacancy centers in photonic crystal cavities in diamond,” *Appl. Phys. Lett.*, vol. 106, no. 22, p. 221103, Jun. 2015, doi: 10.1063/1.4922117.
- [29] M. W. Doherty, N. B. Manson, P. Delaney, F. Jelezko, J. Wrachtrup, and L. C. L. Hollenberg, “The nitrogen-vacancy colour centre in diamond,” *Physics Reports*, vol. 528, no. 1. North-Holland, pp. 1–45, Jul. 01, 2013, doi: 10.1016/j.physrep.2013.02.001.
- [30] N. B. Manson and J. P. Harrison, “Photo-ionization of the nitrogen-vacancy center in diamond,” *Diam. Relat. Mater.*, vol. 14, no. 10, pp. 1705–1710, Oct. 2005, doi: 10.1016/j.diamond.2005.06.027.
- [31] R. Albrecht, A. Bommer, C. Deutsch, J. Reichel, and C. Becher, “Coupling of a Single Nitrogen-Vacancy Center in Diamond to a Fiber-Based Microcavity,” *Phys. Rev. Lett.*, vol. 110, no. 24, p. 243602, Jun. 2013, doi: 10.1103/PhysRevLett.110.243602.
- [32] J. S. Jensen and O. Sigmund, “Topology optimization for nano-photonics,” *Laser Photon. Rev.*, vol. 5, no. 2, pp. 308–321, Mar. 2011, doi: 10.1002/lpor.201000014.
- [33] D. Sell, J. Yang, S. Doshay, R. Yang, and J. A. Fan, “Large-Angle, Multifunctional Metagratings Based on Freeform Multimode Geometries,” *Nano Lett.*, vol. 17, no. 6, pp. 3752–3757, Jun. 2017, doi: 10.1021/acs.nanolett.7b01082.
- [34] E. W. Wang, D. Sell, T. Phan, and J. A. Fan, “Robust design of topology-optimized metasurfaces,” 2019, doi: 10.1364/OME.9.000469.

- [35] “Lumerical Inc.” [Online]. Available: <https://www.lumerical.com/products/>.
- [36] C. M. Lalau-Keraly, S. Bhargava, O. D. Miller, and E. Yablonovitch, “Adjoint shape optimization applied to electromagnetic design,” *Opt. Express*, vol. 21, no. 18, p. 21693, Sep. 2013, doi: 10.1364/OE.21.021693.
- [37] O. Sigmund, “Manufacturing tolerant topology optimization,” *Acta Mech. Sin.*, vol. 25, no. 2, pp. 227–239, Apr. 2009, doi: 10.1007/s10409-009-0240-z.
- [38] T. W. Hughes, M. Minkov, I. A. D. Williamson, and S. Fan, “Adjoint Method and Inverse Design for Nonlinear Nanophotonic Devices,” *ACS Photonics*, vol. 5, no. 12, pp. 4781–4787, Dec. 2018, doi: 10.1021/acsphotonics.8b01522.
- [39] D. Sell, J. Yang, S. Doshay, R. Yang, and J. A. Fan, “Large-Angle, Multifunctional Metagratings Based on Freeform Multimode Geometries,” *Nano Lett.*, vol. 17, no. 6, pp. 3752–3757, Jun. 2017, doi: 10.1021/acs.nanolett.7b01082.
- [40] J. Andkjær, V. E. Johansen, K. S. Friis, and O. Sigmund, “Inverse design of nanostructured surfaces for color effects,” *J. Opt. Soc. Am. B*, vol. 31, no. 1, p. 164, Jan. 2014, doi: 10.1364/josab.31.000164.
- [41] J. Lu and J. Vučković, “Nanophotonic computational design,” *Opt. Express*, vol. 21, no. 11, p. 13351, Jun. 2013, doi: 10.1364/oe.21.013351.
- [42] A. Y. Piggott, J. Lu, K. G. Lagoudakis, J. Petykiewicz, T. M. Babinec, and J. Vučković, “Inverse design and demonstration of a compact and broadband on-chip wavelength demultiplexer,” *Nat. Photonics*, vol. 9, no. 6, pp. 374–377, Jun. 2015, doi: 10.1038/nphoton.2015.69.
- [43] D. X. Xu *et al.*, “Silicon photonic integration platform-Have we found the sweet spot?,” *IEEE J. Sel. Top. Quantum Electron.*, vol. 20, no. 4, Jul. 2014, doi: 10.1109/JSTQE.2014.2299634.
- [44] H. Yang *et al.*, “Transfer-printed stacked nanomembrane lasers on silicon,” *Nat. Photonics*, vol. 6, no. 9, pp. 615–620, Sep. 2012, doi: 10.1038/nphoton.2012.160.
- [45] P. Goy, J. M. Raimond, M. Gross, and S. Haroche, “Observation of cavity-enhanced single-atom spontaneous emission,” *Phys. Rev. Lett.*, vol. 50, no. 24, pp. 1903–1906, Jun. 1983, doi: 10.1103/PhysRevLett.50.1903.
- [46] M. Parikh, “Corrections to proximity effects in electron beam lithography. I. Theory,” *J. Appl. Phys.*, vol. 50, no. 6, pp. 4371–4377, Jun. 1979, doi: 10.1063/1.326423.
- [47] T. M. Babinec *et al.*, “A diamond nanowire single-photon source,” *Nat. Nanotechnol.*, vol. 5, no. 3, pp. 195–199, Feb. 2010, doi: 10.1038/nnano.2010.6.
- [48] I. Bulu, T. Babinec, B. Hausmann, J. T. Choy, and M. Loncar, “Plasmonic resonators for enhanced diamond NV- center single photon sources,” *Opt. Express*, vol. 19, no. 6, p. 5268, Mar. 2011, doi: 10.1364/oe.19.005268.
- [49] J. T. Choy, I. Bulu, B. J. M. Hausmann, E. Janitz, I.-C. Huang, and M. Lončar, “Spontaneous emission and collection efficiency enhancement of single emitters in diamond via plasmonic cavities and gratings,” *Appl. Phys. Lett.*, vol. 103, no. 16, p. 161101, Oct. 2013, doi: 10.1063/1.4817397.
- [50] A. Karamlou, M. E. Trusheim, and D. Englund, “Metal-dielectric antennas for efficient photon collection from diamond color centers,” *Opt. Express*, vol. 26, no. 3, p. 3341, Feb. 2018, doi: 10.1364/oe.26.003341.

- [51] C. W. Cheng, K. T. Shiu, N. Li, S. J. Han, L. Shi, and D. K. Sadana, “Epitaxial lift-off process for gallium arsenide substrate reuse and flexible electronics,” *Nat. Commun.*, vol. 4, no. 1, pp. 1–7, Mar. 2013, doi: 10.1038/ncomms2583.
- [52] M. Atatüre, D. Englund, N. Vamivakas, S. Y. Lee, and J. Wrachtrup, “Material platforms for spin-based photonic quantum technologies,” *Nature Reviews Materials*, vol. 3, no. 5. Nature Publishing Group, pp. 38–51, May 01, 2018, doi: 10.1038/s41578-018-0008-9.
- [53] M. K. Boll, I. P. Radko, A. Huck, and U. L. Andersen, “Photophysics of quantum emitters in hexagonal boron-nitride nano-flakes,” *Opt. Express*, vol. 28, no. 5, p. 7475, Mar. 2020, doi: 10.1364/oe.386629.

Supplemental information:

Adjoint-optimized nanoscale light extractor for nitrogen-vacancy centers in diamond

Raymond A. Wambold¹, Zhaoning Yu^{1,2}, Yuzhe Xiao¹, Benjamin Bachman³, Gabriel Jaffe², Shimon Kolkowitz², Jennifer T. Choy^{4,1,5}, Mark Eriksson², Robert J. Hamers³, Mikhail A. Kats^{1,2,5}

1. Department of Electrical and Computer Engineering, University of Wisconsin – Madison

2. Department of Physics, University of Wisconsin – Madison

3. Department of Chemistry, University of Wisconsin – Madison

4. Department of Engineering Physics, University of Wisconsin – Madison

5. Department of Materials Science and Engineering, University of Wisconsin - Madison

S1. Near-field comparison with and without the NLE

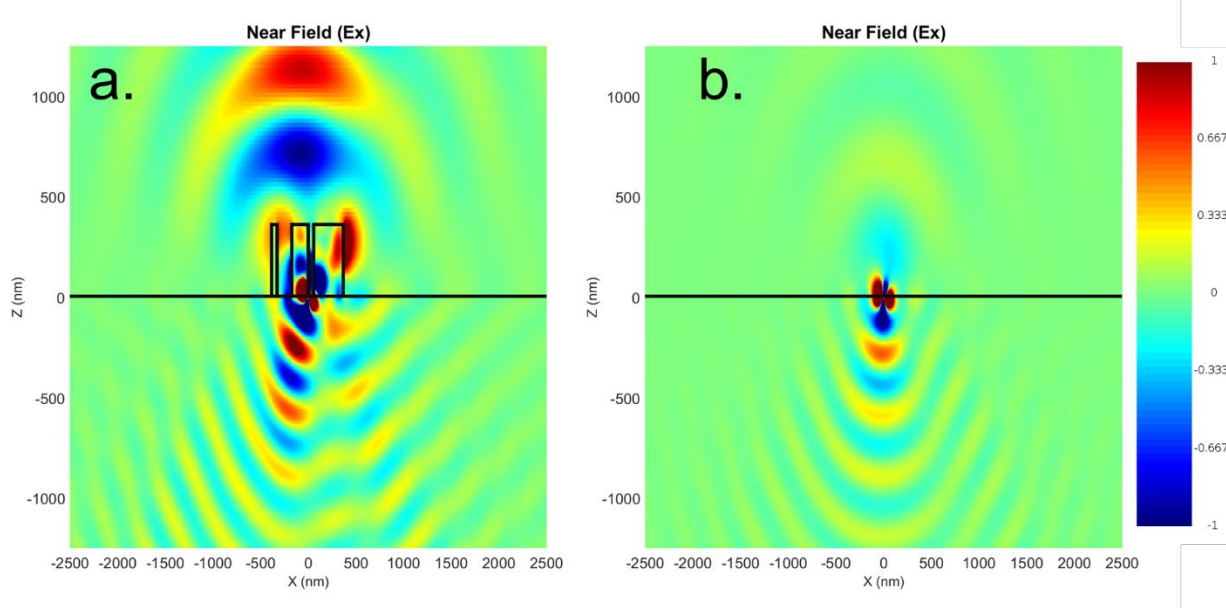


Figure S1. The x-component of a snapshot of the electric field in the vicinity of the NV center taken along a slice in the XZ plane at $y = 0$ (the center of the device and the y-coordinate of the NV), at a wavelength of 675 nm. Here we directly compare the field with **(a)** and without **(b)** the NLE. The structure is outlined in black for reference.

S2. FoM vs. the NLE angle with respect to the NV orientation

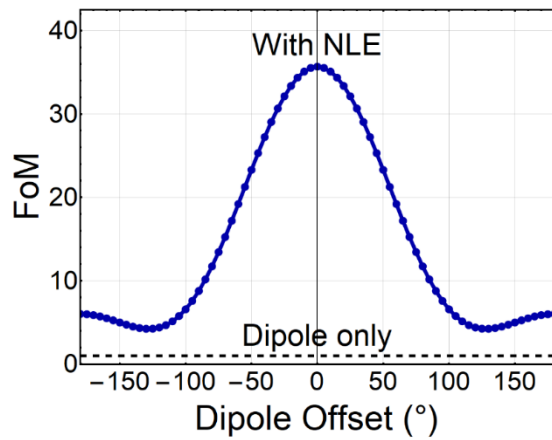


Figure S2. The full rotational robustness of the NLE demonstrated by rotating the NV emitter a full 360° around the Z axis.

S3. Far-field $|E|^2$ plots for select wavelengths across 635 – 800 nm

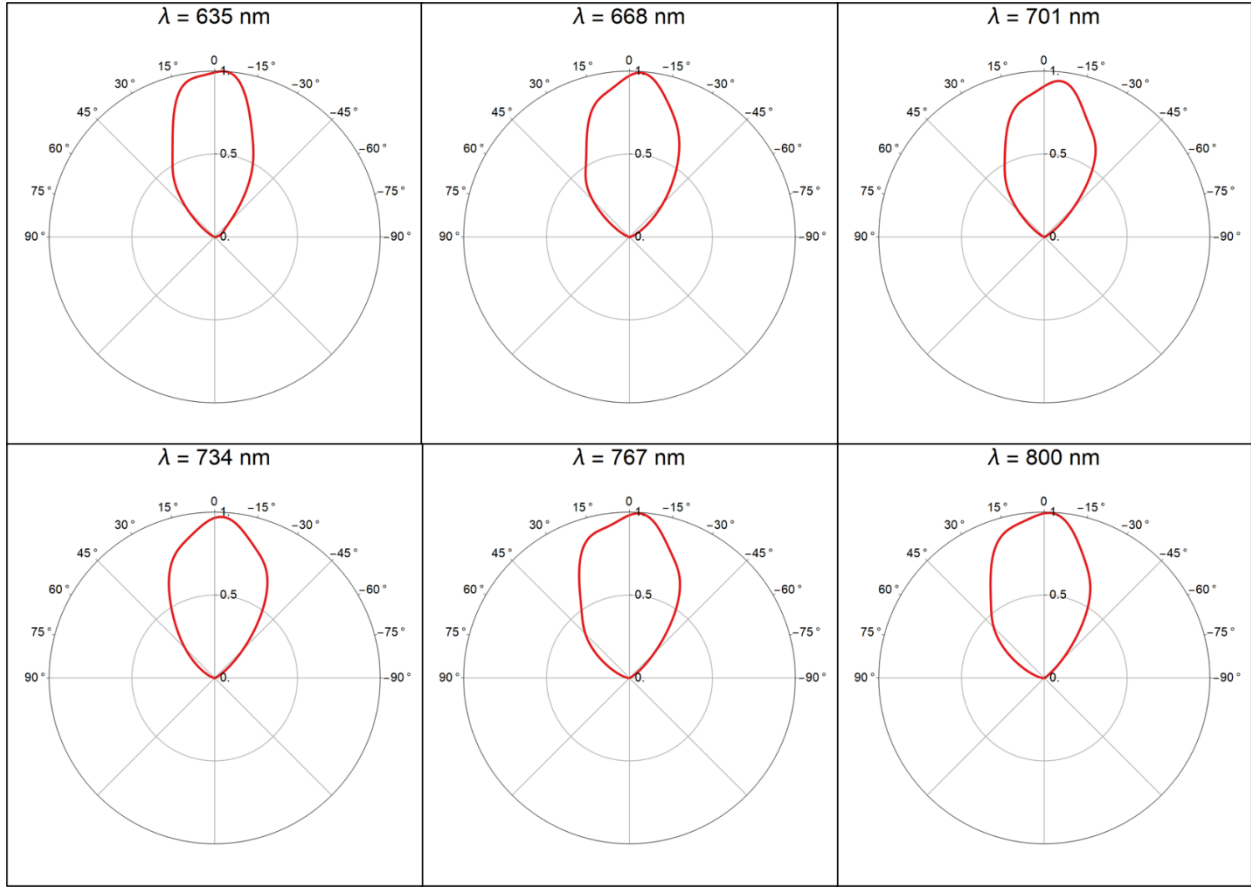


Figure S3. To make sure the beaming capabilities of our device are maintained over the full 635 – 800 nm spectrum we simulated and calculated the far-field $|E|^2$ intensities for multiple other wavelengths besides the one presented in Figure 3(d). Here we plot slices of the field profiles at an azimuthal angle of 0° and along a polar angle of $\pm 90^\circ$ for wavelengths 635, 668, 701, 734, 767, and 800 nm. The far-fields are normalized to the peak intensity over the full hemispherical projection ($-90^\circ \leq \theta \leq 90^\circ$ and $0^\circ \leq \varphi \leq 360^\circ$) so the peaks in some plots occur at another azimuthal angle. The peak intensity always stays within $\pm 15^\circ$ of the normal with only minor variations between the different wavelengths.

S4. Alternative designs

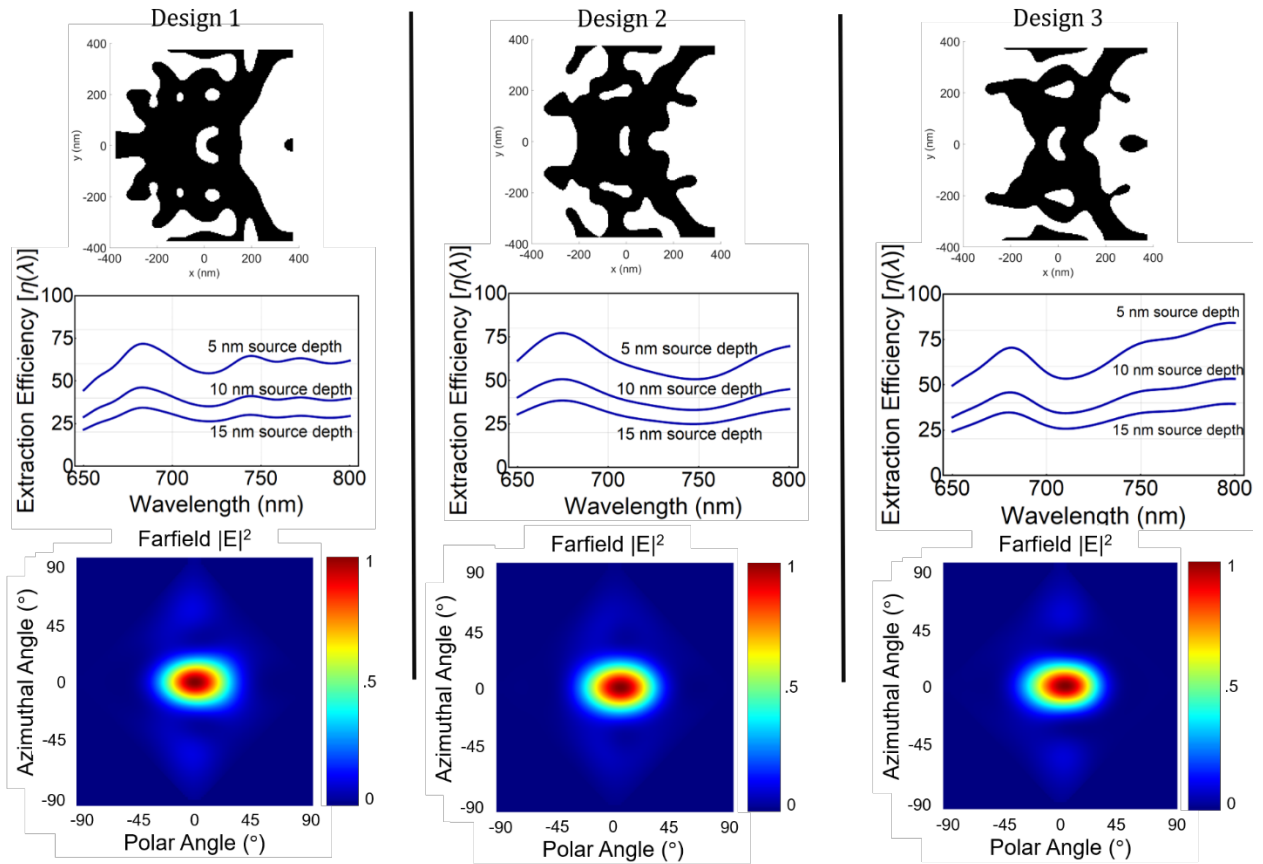


Figure S4. Early designs found during this project. It is interesting to compare the overall features of each design side by side and note key structural similarities between them, namely an arced cavity where the dipole is located and similar guiding features to the sides. While the FoMs are quite good here, these structures have severe aspect ratios and small features sizes, making fabrication much more difficult compared to the NLE presented in the main text.